Field Computations Through the ACA Algorithm

Field Computations Through the ACA Algorithm

Rob Maaskant[1], Vito Lancelotti[2]
[1]Chalmers University of Technology, Gothenburg, Sweden, rob.maaskant@chalmers.se
[2]Eindhoven University of Technology, Eindhoven, The Netherlands, v.lancelotti@tue.nl

***Abstract*—The adaptive cross approximation algorithm is invoked for the fast construction of the method-of-moment matrix involving source basis functions for the currents and a set of auxiliary test functions that samples the radiated electromagnetic (EM) field. Once the adaptive cross approximation coupling matrix is constructed, the far and near fields from a source current are obtained directly through a single matrix-vector product. The post-processing method is particularly fast when the EM fields are smoothly varying over their sampling domain, or when far fields need to be computed for many current distributions, e.g., for sets of macro basis functions arising in several domain decomposition methods.**

***Index Terms*—ACA algorithm, far field, near field, moment method.**

I. Introduction

The adaptive cross approximation (ACA) algorithm, first introduced in [1], has been used extensively to accelerate the numerical discretization of electromagnetic field integral equations; more specifically, this purely algebraic method has been used in moment method approaches, both for the compression and for the fast construction of low-rank off-diagonal moment matrix (MoM) blocks [2]–[5]. This paper proposes to use the ACA algorithm as a post-processing step, namely for the fast computation of the far and near fields of radiating structures. Micro scale basis functions are used as localized field testing functions at the desired field sampling points after which the ACA-generated MoM matrix is constructed between these field testing functions and the basis functions for modeling the current. Once the currents on the radiating structure are known, the corresponding EM fields are obtained algebraically through matrix-vector products. The method is particularly fast when the fields are smoothly varying over its sampling domain and when fields need to be computed for many current distributions, e.g. for sets of macro basis functions as is the case in several domain decomposition methods. An additional advantage is that an existing MoM solver can be used directly for the post-processing of the fields, while benefiting from MoM acceleration techniques, which is also more consistent as the same solver is used for both the computation of the currents and the fields through the appropriate Green's functions. Finally, a recent application of the ACA algorithm in computing equivalent currents (basically near fields) on an equivalent outer surface enclosing an inner equivalent source surface can be found in [6], the field sampling method of which has some commonality with the present work.

Section II details the ACA field computation concept for a simple example. The computation of the radiating fields of a single Bowtie antenna element will be examined in Sec. III. Since the method applies to both electric and magnetic fields/currents, a slot antenna array example is considered afterwards. Conclusions are drawn in Sec. IV.

II. ACA Field Computations

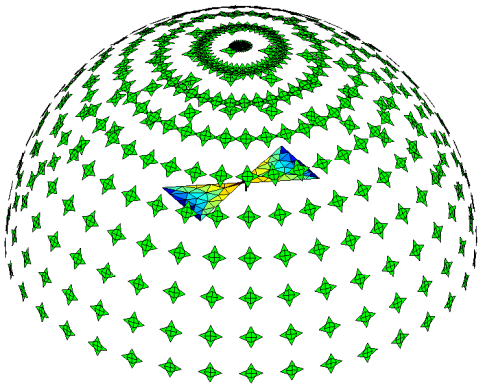

Fig. 1. EM field sampling of a radiating Bowtie antenna element. The field sampling RWGs are enlarged for vizualization purposes.

Fig. 1 illustrates a Bowtie antenna element above a PEC ground plane whose radiated EM fields are tested onto pairs of orthogonally-oriented Rao-Wilton-Glisson (RWG) basis functions that are placed tangential to a hemispherical surface surrounding the antenna. Note that this setup is equivalent to performing measurements with a near field scanner although the field sampling RWGs can have any desired orientation and position as shown later. The RWGs must be chosen small enough to be able to assume that the field is tested at a single point only. Also, the testing RWGs are allowed to overlap and/or intersect.

As an example, let Z_{mn} denote the reaction between the E-field of the source electric current RWG basis function $\boldsymbol{f}_n$ and the RWG testing function $\boldsymbol{f}_m$, then

$$Z_{mn} = \int_{S_m} \boldsymbol{f}_m \cdot \boldsymbol{E}(\boldsymbol{f}_n) \mathrm{d}S \tag{1}$$

where S_m is the support of the RWG testing function $\boldsymbol{f}_m$, and where

$$\boldsymbol{f}_m = \begin{cases} \dfrac{\ell_m}{2A_m^{\pm}} \boldsymbol{\rho}_m^{\pm} & \boldsymbol{r} \in T_m^{\pm} \\ \boldsymbol{0} & \text{elsewhere.} \end{cases} \tag{2}$$

Here, $\boldsymbol{\rho}_m^{\pm} = \pm(\boldsymbol{r} - \boldsymbol{r}_{m,0}^{\pm})$, $T_m^{\pm}$ are the triangular supports of the mth RWG, $\boldsymbol{r}_{m,0}^{\pm}$ are the corresponding free corner vertices, and ℓ_m is the mth RWG common edge length. Next, upon assuming identical RWG testing triangles that are in the same plane, i.e., $A_m^{\pm} = A$, $\boldsymbol{\rho}_m^{\pm} = \boldsymbol{\rho}_m$, and also that $\ell_m = \ell$, and by evaluating (1) through the midpoint integration rule at the triangle centroids $\boldsymbol{r}_{m,\mathrm{c}}^{\pm}$, yields

$$Z_{mn} = \frac{\ell \boldsymbol{\rho}_m}{2} \cdot \left[\boldsymbol{E}(\boldsymbol{r}_{m,\mathrm{c}}^{+}) + \boldsymbol{E}(\boldsymbol{r}_{m,\mathrm{c}}^{-}) \right]. \tag{3}$$

Furthermore, if the mth RWG that samples the field is sufficiently small, we can assume that $\boldsymbol{E}(\boldsymbol{r}_{m,\mathrm{c}}^{+}) \approx \boldsymbol{E}(\boldsymbol{r}_{m,\mathrm{c}}^{-})$. If we further choose that $\boldsymbol{\rho}_m = \ell \hat{\boldsymbol{\rho}}_m$, and if the expansion coefficient for basis function $\boldsymbol{f}_n$ is known to be I_n, we conclude from (3) that

$$E_{\rho_m}(\boldsymbol{r}_m) = \ell^{-2} Z_{mn} I_n \tag{4}$$

where $\boldsymbol{r}_m = (\boldsymbol{r}_{m,\mathrm{c}}^{+} + \boldsymbol{r}_{m,\mathrm{c}}^{-})/2$. In other words, (4) shows how the ρ_m component of the E-field at the point $\boldsymbol{r}_m$ radiated by basis function $\boldsymbol{f}_n$ of strength I_n is given through the MoM matrix element Z_{mn}.

After building the total coupling matrix $\mathbf{Z}$, and given the solution expansion coefficient vector $\mathbf{J} = [I_1, I_2, \ldots, I_N]^T$, we obtain for the total field $\mathbf{V} = \mathbf{ZJ}$, which, on account of (4), is seen to be directly related to the total radiated E-field through

$$\mathbf{E} = \ell^{-2}\mathbf{ZJ} \approx \ell^{-2}\mathbf{Q}\,(\mathbf{UJ}) \tag{5}$$

where the column-vector $\mathbf{E}$ holds the polarization-sampled E-field values, and where the ACA algorithm is used in the process of computing the low-rank block factorization of $\mathbf{Z}$, i.e., $\mathbf{Z} = \mathbf{QU}$. [1]This is done iteratively, where the ACA threshold κ is set to control the approximation error: $\kappa = \|\mathbf{QU} - \mathbf{Z}\|_F / \|\mathbf{Z}\|_F$, where F denotes the Frobenius-norm. Typical values for κ range from 10^{-2} to 10^{-3}. The number of iterations, which is also the number of columns in $\mathbf{Q}$, equals the matrix effective rank.

Although the above electric field is solely generated by an electric current, *viz.* $\boldsymbol{E}(\boldsymbol{J})$, for linear reacting systems we generally have that

$$\boldsymbol{E}(\boldsymbol{J}, \boldsymbol{M}) = \boldsymbol{E}(\boldsymbol{J}) + \boldsymbol{E}(\boldsymbol{M}) \tag{6a}$$
$$\boldsymbol{H}(\boldsymbol{J}, \boldsymbol{M}) = \boldsymbol{H}(\boldsymbol{J}) + \boldsymbol{H}(\boldsymbol{M}) \tag{6b}$$

for the total electric and magnetic fields, respectively. Furthermore, when near fields are considered, one is often interested in the three Cartesian components of the vector field. Accordingly, one can employ the three orthogonally-oriented field sampling RWG functions as shown in Fig. 2 (see also [6]). Similar to the derivation leading up to (5), the E- and H-fields are then computed in general as

$$\mathbf{E} = \ell^{-2} \left[\mathbf{Z}^{EJ}\mathbf{J} + \mathbf{Z}^{EM}\mathbf{M} \right] \tag{7a}$$
$$\mathbf{H} = \ell^{-2} \left[\mathbf{Z}^{HJ}\mathbf{J} + \mathbf{Z}^{HM}\mathbf{M} \right] \tag{7b}$$

[1]The evaluation of $\mathbf{Q}(\mathbf{UJ})$ is computationally cheaper than $(\mathbf{QU})\mathbf{J}$.

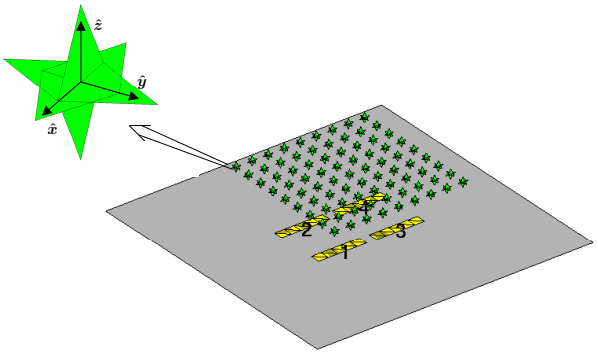

Fig. 2. A set of three orthogonally-oriented field sampling RWG functions (top-left) placed in a rectangular grid above a 2×2 array of slot antennas located in a PEC ground plane.

where the matrix $\mathbf{Z}_{HJ}$, for instance, represents the coupling matrix from the source current RWGs expanding $\boldsymbol{J}$ to the field sampling RWGs testing $\boldsymbol{H}$. Each of the coupling matrices are approximated through the ACA algorithm as in (5).

III. Numerical Results

In the following two examples we examine both the performance and accuracy characteristics of the ACA algorithm in computing the E-field, which is either radiated by an electric or magnetic current source. By doing so, we separately examine the ACA performances of the so-called $\mathcal{L}$- and $\mathcal{K}$-operators, since $\boldsymbol{E}(\boldsymbol{J}, \boldsymbol{M}) = \mathcal{L}(\boldsymbol{J}) - \mathcal{K}(\boldsymbol{M})$, where

$$\mathcal{L}(\boldsymbol{J}) = -j\omega\mu \left[\int_{\mathcal{V}} \boldsymbol{J}(\boldsymbol{r}') G(\boldsymbol{r}, \boldsymbol{r}') \mathrm{d}V' + \frac{1}{k^2} \int_{\mathcal{V}} \boldsymbol{\nabla}' \cdot \boldsymbol{J}(\boldsymbol{r}') \boldsymbol{\nabla} G(\boldsymbol{r}, \boldsymbol{r}') \mathrm{d}V' \right] \tag{8a}$$

$$\mathcal{K}(\boldsymbol{M}) = \int_{\mathcal{V}} \boldsymbol{M}(\boldsymbol{r}') \times \boldsymbol{\nabla}' G(\boldsymbol{r}, \boldsymbol{r}') \mathrm{d}V'. \tag{8b}$$

A. Radiated E-Field from a Bowtie Antenna

The E-field of a resonant $\lambda/2$ Bowtie antenna placed $\lambda/4$ above a PEC ground plane, as shown in Fig. 1, is considered first. The field sampling RWGs are placed tangential to the surface of a hemisphere of radius R. For large R, one could let the length ℓ of these RWGs scale with R to compensate for the R^{-1} decay of the field to maintain high numerical accuracy when computing Z_{mn} through a MoM approach.

Using (5), we will examine the normalized field function

$$G(R, \theta, \phi) = \frac{2\pi}{\eta P_{\mathrm{in}}} |\boldsymbol{E}_{\tan}(R, \theta, \phi) R e^{jkR}|^2 \tag{9}$$

where P_{in} is the antenna input power, η is the free-space impedance, and k is the corresponding wavenumber. Note that, if $R \to \infty$, one observes that $G(R, \theta, \phi) \to G(\theta, \phi)$, i.e., G turns into the ordinary far-field function.

We further consider the computational accuracy and efficiency for various ACA threshold levels κ relative to a direct calculation through $\mathbf{Z}$ in (5), which constitutes our reference solution. We also examine the effect of taking various angular

ranges $0 \leq \theta \leq \theta_0$, where θ_0 is the semi-subtended angle. Finally, the angular resolution of the field sampling grid is fixed: $\Delta\theta = \Delta\phi = 5$ degrees, and the relative average field error is computed as

$$\epsilon_{\%} = \frac{\int_{\theta<\theta_0} |\boldsymbol{E}_{\tan,\mathrm{ref}} - \boldsymbol{E}_{\tan}|^2 \mathrm{d}\Omega}{\int_{\theta<\theta_0} |\boldsymbol{E}_{\tan,\mathrm{ref}}|^2 \mathrm{d}\Omega} \times 100\%. \qquad (10)$$

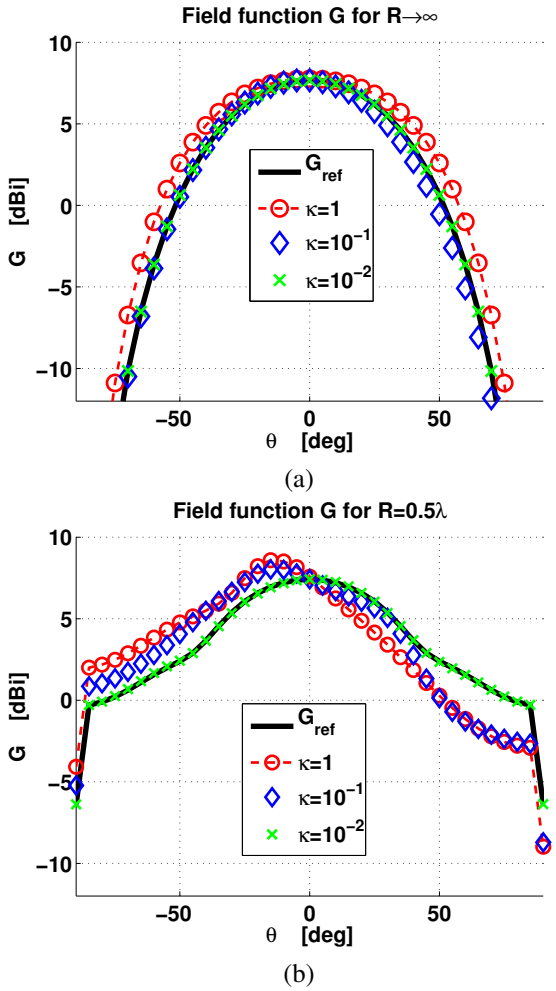

Fig. 3. E-plane field function G computed for different ACA threshold levels, for: (a) $R \to \infty$, and; (b) $R = 0.5\lambda$.

Fig. 3(a) shows that the numerical accuracy of the computed E-plane far-field function is weakly dependent on the ACA threshold κ. The accuracy increases for smaller ACA threshold values. Note in Fig. 3(b) that the ACA threshold must be chosen much smaller in the near field ($R = 0.5\lambda$) to obtain accurate results. Further note that the ACA factorization in (5) is performed by selecting rows and columns of $\mathbf{Z}$, so if this procedure is terminated prematurely, asymmetry in the field pattern may arise as visualized in Fig. 3(b) for $\kappa > 10^{-2}$. The matrix $\mathbf{Z}$ is non-square viz. of size 2774×101, which may negatively impact the numerical speed-up of the ACA field computations. In fact, for $R \to \infty$ the speed-up factors are 18 ($\kappa = 1$), 2.0 ($\kappa = 10^{-1}$), and 1.3 ($\kappa = 10^{-2}$), while for $R = 0.5\lambda$ these are 19 ($\kappa = 1$), 3.3 ($\kappa = 10^{-1}$), and 0.5 ($\kappa = 10^{-2}$).

B. Radiated E-Field from Slot Antennas

As the second example, we consider the 2×2 array of $\lambda/2$ radiating slot antennas located in a PEC ground plane as shown in Fig. 2. Each slot assumes a TE_{10} waveguide mode with equal excitation amplitudes (1 V/m in the slot center) in order to scan to broadside ($\theta = 0$). The slot modal field is generated by an equivalent magnetic current that is placed right above the ground plane and is synthesized by RWG basis functions. The slot width is $\lambda/10$, which is also equal to the H-plane gap separation between the slots (*cf.* Fig. 2). Both the E- and

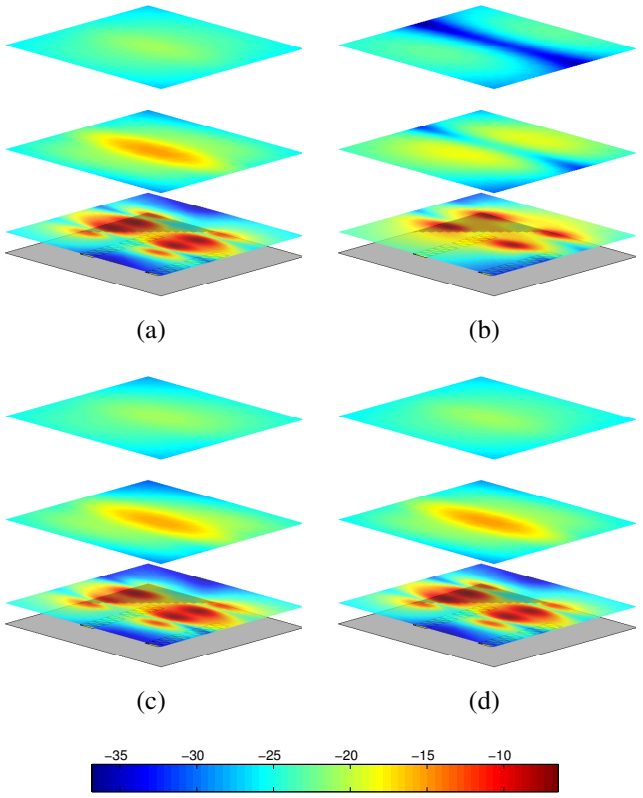

Fig. 4. Radiated E-field of a 2×2 array of slots whose near-field is sampled in the planes $z \in \{0.1\lambda, 0.5\lambda, 1.0\lambda\}$ in front of the array (dBV/m). (a) Reference case ($\kappa = 0$); (b) ACA threshold $\kappa = 10^0$; (c) ACA threshold $\kappa = 10^{-1}$; (d) ACA threshold $\kappa = 10^{-2}$.

H-fields are sampled by RWG testing functions, as in Fig. 2, in planes in front of the array for different ACA threshold levels. The field sampling resolution is $\Delta x = \Delta y = \lambda/30$, $\ell = 1E-10$ m, and the mesh discretization in the slot is $\lambda/10$.

As can be concluded from Fig. 4, the field $|\boldsymbol{E}(\boldsymbol{M})|$ exhibits strong asymmetries for the highest ACA threshold level, i.e., $\kappa = 10^0$, whereas the error in the field decreases for smaller threshold levels relative to the reference case in Fig. 4(a). This behavior is expected and also similar to the above-described

Bowtie antenna example. The field is visually indistinguishable from the reference solution in the last case, Fig. 4(d).

The singular value spectra of $\mathbf{Z}^{EM}$ are shown in Fig. 5 for different cases. One observes that the effective matrix rank decreases as the sampling plane moves away from the source currents, as expected. Furthermore, it can be seen that if the slots are meshed more finely ($\lambda/40$ instead of $\lambda/10$ mesh size), the coupling matrix will be more rank-deficient and the use of the ACA algorithm will have clearer benefits over a direct matrix fill approach.

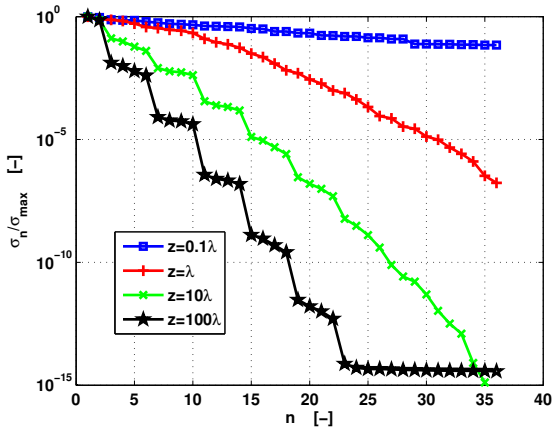

(a)

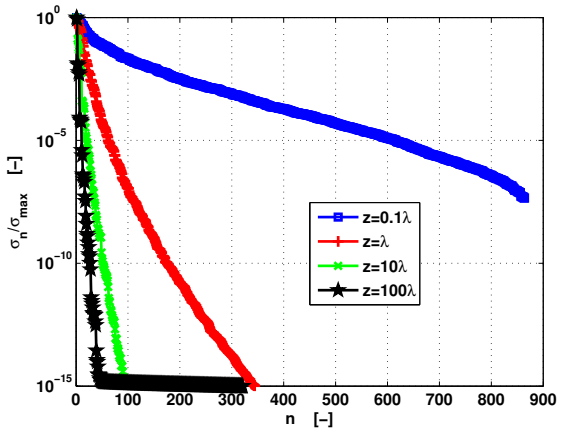

(b)

Fig. 5. Singular value spectra of $\mathbf{Z}^{EM}$ for the sampling plane distances $z = 0.1\lambda$,$z = \lambda$, $z = 10\lambda$, and $z = 100\lambda$. (a) Size $\mathbf{Z}^{EM}$ is 7437×36 ($\lambda/10$ slot meshing); (b) Size $\mathbf{Z}^{EM}$ is 7437×864 ($\lambda/40$ slot meshing).

Table I summarizes the numerical values for both the E- and H-field errors as well as the speed-up factor relative to a direct approach (no ACA) for different ACA threshold levels, sampling plane distances, and mesh sizes of the slots. For this specific slot array example, the speed-up factor is as large as 89 for $\kappa = 10^0$,$z = 0.1\lambda$, and $\lambda/10$ meshing, but the field computations suffer from large errors. On the other hand, 0% error level can be achieved for $\kappa = 10^{-2}$, even in the reactive field, but then the ACA algorithm is much slower than a direct matrix fill approach as the matrix block is barely rank-deficient. Moving the sampling plane away and increasing the mesh density for the slots is beneficial for the ACA approach (see also Fig. 5); the error is seen to be less than 10% for $\kappa = 10^{-2}$, $z = 100\lambda$ and for a $\lambda/40$ meshing.

TABLE I
ACCURACY AND EFFICIENCY OF THE NEAR FIELD COMPUTATIONS

$z = 0.1\lambda$, $\lambda/10$ mesh	$\kappa = 0$	$\kappa = 10^0$	$\kappa = 10^{-1}$	$\kappa = 10^{-2}$
$\epsilon^E_\%$	0.0	579	114	0.0
$\epsilon^H_\%$	0.0	502	105	0.0
Speed-up factor	1.0	9.8	0.32	0.14
$z = 100\lambda$, $\lambda/10$ mesh	$\kappa = 0$	$\kappa = 10^0$	$\kappa = 10^{-1}$	$\kappa = 10^{-2}$
$\epsilon^E_\%$	0.0	31866	58	58
$\epsilon^H_\%$	0.0	50	57	4.2
Speed-up factor	1.0	9.4	0.75	0.62
$z = 0.1\lambda$, $\lambda/40$ mesh	$\kappa = 0$	$\kappa = 10^0$	$\kappa = 10^{-1}$	$\kappa = 10^{-2}$
$\epsilon^E_\%$	0.0	27568	429	28
$\epsilon^H_\%$	0.0	349	224	12
Speed-up factor	1.0	89	8.8	0.69
$z = 100\lambda$, $\lambda/40$ mesh	$\kappa = 0$	$\kappa = 10^0$	$\kappa = 10^{-1}$	$\kappa = 10^{-2}$
$\epsilon^E_\%$	0.0	41788	5	8.3
$\epsilon^H_\%$	0.0	56	27	10
Speed-up factor	1.0	84	13	10

IV. Conclusion

The ACA algorithm has been applied for computing the near and far fields of radiating structures; a Bowtie antenna and an array of slots in a ground plane have been examined and the performance of the novel field post-processing algorithm has been analyzed. The accuracy and numerical efficiency of the method are as one can expect based on the effective rank of the moment matrix describing the coupling between the source basis functions and the field testing functions. This needs to be explored further, as well as how the method can be integrated in domain decomposition methods as it is particularly fast for computing fields from multiple source currents through simple matrix vector products.

Acknowledgment

We thank the support of the Swedish Research Council.

References

[1] M. Bebendorf, "Approximation of boundary element matrices," *Numer. Math.*, vol. 86, no. 4, pp. 565–589, Jun. 2000.

[2] S. Kurz, O. Rain, and S. Rjasanow, "The adaptive cross-approximation technique for the 3-D boundary-element method," *IEEE Trans. Magn.*, vol. 38, no. 2, pp. 421–424, Mar. 2002.

[3] K. Zhao, M. N. Vouvakis, and J. F. Lee, "The adaptive cross approximation algorithm for accelerated method of moments computations of EMC problems," *IEEE Trans. Electromagn. Compat.*, vol. 47, no. 4, pp. 763–773, Nov. 2005.

[4] R. Maaskant, R. Mittra, and A. G. Tijhuis, "Fast analysis of large antenna arrays using the characteristic basis function method and the adaptive cross approximation algorithm," *IEEE Trans. Antennas Propag.*, vol. 56, no. 11, pp. 3440–3451, Nov. 2008.

[5] J. M. Tamayo, A. Heldring, and J. M. Rius, "Multilevel adaptive cross approximation (MLACA)," *IEEE Trans. Antennas Propag.*, vol. 59, no. 12, pp. 4600–4608, Dec. 2011.

[6] M. Li, M. Francavilla, F. Vipiana, G. Vecchi, and R. Chen, "Nested equivalent source approximation for the modeling of multiscale structures," *IEEE Trans. Antennas Propag.*, vol. 62, no. 7, pp. 3664–3678, Jul. 2014.